



Crystallization of interleukin-18 for structure-based inhibitor design

Brian Krumm,^{a,*} Xiangzhi Meng,^b Yan Xiang^b and Junpeng Deng^a^aDepartment of Biochemistry and Molecular Biology, Oklahoma State University, Stillwater, OK 74078, USA, and^bDepartment of Microbiology and Immunology, University of Texas Health Science Center at San Antonio, 7703 Floyd Curl Drive, San Antonio, TX 78229, USA. *Correspondence e-mail: brian.krumm@nih.gov

Received 16 January 2015

Accepted 6 April 2015

Edited by S. W. Suh, Seoul National University, Korea

‡ Current address: Membrane Protein Structure Function Unit, NINDS, National Institutes of Health, Department of Health and Human Services, Rockville, MD 20852, USA.

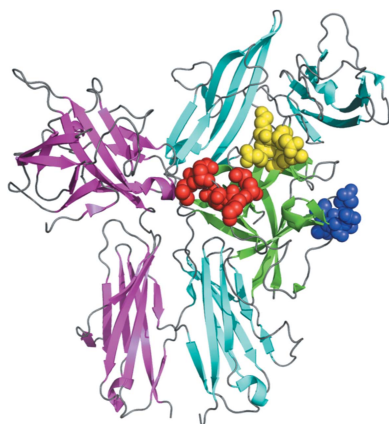
Keywords: cytokines; interleukin-18; immune defense; surface-entropy reduction.**PDB references:** interleukin-18, SER mutant I, 4xfs; SER mutant III, 4xft; SER mutant V, 4xfu**Supporting information:** this article has supporting information at journals.iucr.org/f

Interleukin-18 (IL-18) is a pleiotropic pro-inflammatory cytokine belonging to the IL-1 superfamily. IL-18 plays an important role in host innate and acquired immune defense, with its activity being modulated *in vivo* by its naturally occurring antagonist IL-18 binding protein (IL-18BP). Recent crystal structures of human IL-18 (hIL-18) in complex with its antagonist or cognate receptor(s) have revealed a conserved binding interface on hIL-18 representing a promising drug target. An important step in this process is obtaining crystals of apo hIL-18 or hIL-18 in complex with small-molecule inhibitors, preferably under low ionic strength conditions. In this study, surface-entropy reduction (SER) and rational protein design were employed to facilitate the crystallization of hIL-18. The results provide an excellent platform for structure-based drug design.

1. Introduction

Interleukin-18 (IL-18) is a pleiotropic pro-inflammatory cytokine belonging to the IL-1 superfamily (Dinarello, 1999*a,b*; Okamura *et al.*, 1995). IL-18 plays an important role in both innate and acquired immune responses by inducing interferon- γ (IFN- γ) production from T lymphocytes and macrophages, while also enhancing the cytotoxicity of natural killer cells (Dinarello, 1999*a*). Increased levels of mature IL-18 have a direct correlation with the severity of certain autoimmune diseases such as multiple sclerosis (MS), rheumatoid arthritis (RA) and lupus (Boraschi & Dinarello, 2006). IL-18 activity is modulated *in vivo* by a negative-feedback mechanism involving a naturally occurring IL-18 inhibitor, IL-18BP. As an immune-evasion strategy, homologs of IL-18BPs are also encoded by many poxviruses such as *Molluscum contagiosum virus*, orthopoxviruses such as *Variola virus* (the causative agent of smallpox) and yatapoxviruses such as Yaba-like disease virus (YLDV). The recent crystal structures of hIL-18 in complex with *Ectromelia virus* (ectv; Krumm *et al.*, 2008) and YLDV (Krumm *et al.*, 2012) IL-18BP revealed a conserved mechanism of hIL-18 inhibition through direct competition for a common binding site with the hIL-18 primary receptor (hIL-18R α) domain 3 (D3; Tsutsumi *et al.*, 2014; Wei *et al.*, 2014).

From the IL-18BP studies, it was shown that the complex interface between hIL-18 and IL-18BP is comprised of a mixture of charged and hydrophobic residues, but is overall predominantly hydrophobic in nature (Krumm *et al.*, 2008). The crystal structures revealed a pliable surface of hIL-18 that undergoes an induced-fit mechanism upon binding IL-18BPs, involving three ligand-binding sites (A, B and C) on hIL-18 (Krumm *et al.*, 2008, 2012; Figs. 1*a* and 1*b*). Contained within binding site A is a critical hIL-18 lysine residue (Lys53), which when mutated to alanine displayed a greater than 100-fold and



fourfold decrease in binding affinity for *Variola virus* IL-18BP and hIL-18R α , respectively (Meng *et al.*, 2007), indicating that binding site A on the hIL-18 surface is a ‘hot spot’ that is critical not only for its interaction with viral IL-18BPs but also for initial hIL-18–receptor complex formation. Additionally, binding site C on the hIL-18 interface is another potential ‘hot spot’ as it contains a conserved phenylalanine residue that has been shown to be critical for complex formation with orthopoxviruses, *Molluscum contagiosum virus* (MCV) and human

IL-18BP (Esteban & Buller, 2004; Krumm *et al.*, 2012; Xiang & Moss, 2001*a,b*).

The recent crystal structures of binary and ternary complexes of hIL-18 with its receptors have shown that IL-18BP competes directly with the hIL-18R α D3 domain for binding hIL-18, overlapping the previously identified hIL-18 binding site II. Superposition of hIL-18 molecules from the viral IL-18BP complexes and the ternary complex reveals few conformational changes of the core β -trefoil fold, which has an

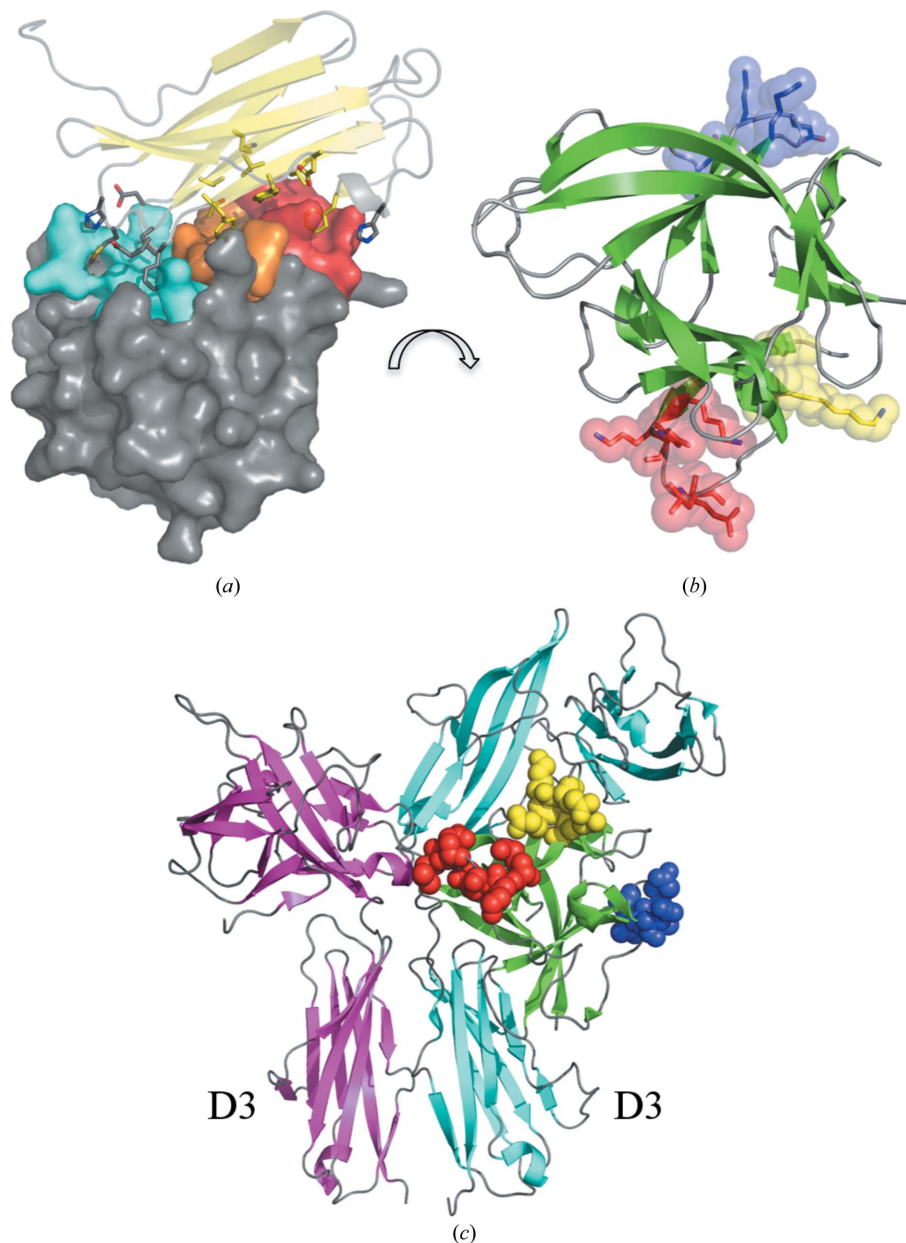


Figure 1

Surface-entropy reduction (SER) clusters on hIL-18. (a) Crystal structure of the ectvIL-18BP–hIL-18 complex (PDB entry 3f62; Krumm *et al.*, 2008). EctvIL-18BP is depicted as a ribbon diagram and is colored light yellow; hIL-18 is shown as a surface representation. Residues of ectvIL-18BP at the interface are shown as sticks interacting with previously identified binding sites on hIL-18 colored as follows: site A, red; site B, orange; site C, cyan. The remaining surface of hIL-18 is colored gray. (b) Crystal structure of hIL-18 from PDB entry 3f62 drawn as a cartoon representation and colored green; ectvIL-18BP has been removed for clarity, revealing the opening of the hIL-18 β -trefoil barrel. (c) Crystal structure of the IL-18 ternary complex shown as a ribbon diagram with IL-18R α in cyan, IL-18R β in magenta and IL-18 in green (PDB entry 3wo4; Tsutsumi *et al.*, 2014). The colored spheres in (b) and (c) are the SER clusters: mutant I, red; mutant II, yellow; mutants III, IV and V, blue. Notice that the mutation sites are distant from the IL-18BP and IL-18R α D3 domain interfaces.

r.m.s. deviation of 0.5–0.6 Å, although several loops show a significant deviation upon interacting with the hIL-18 receptors. Notably different is the buried surface area (BSA) and the number of residues involved in the interface between hIL-18 and the hIL-18R α D3 domain. Site II between hIL-18 and the hIL-18R α D3 domain is relatively small (603 Å²; Wei *et al.*, 2014) when compared with the viral complex interfaces (the ectv and YLDV IL-18BP interfaces have BSAs of 1930 and 1957 Å², respectively; Krumm *et al.*, 2008, 2012). As observed previously in the viral inhibitory complexes, Lys53 of binding site A in hIL-18 adopts a conserved interaction at the binding interface with the receptor. However, in comparison to the hIL-18–hIL-18R α D3 interface, the viral inhibitory proteins contribute many more aromatic and hydrophobic residues to hIL-18 binding, including the conserved phenylalanine of IL-18BP at binding site C. Thus, the identified surface patches on hIL-18 could therefore be further targeted for the design of small-molecule inhibitors that would have the potential to discriminate between IL-18R α and IL-18BP binding in the future.

Protein–protein interactions are associated with many crucial biological processes such as signal transduction, cell adhesion, cellular proliferation, growth and differentiation, while their malfunctions have been identified in numerous pathological disease states. It is estimated that up to 650 000 interactions, termed the ‘interactome’, regulate biological processes within the human cell (Stumpf *et al.*, 2008). While most small-molecule drugs currently on the market are either competitive inhibitors of G protein-coupled receptors, nuclear receptors, ion channels or enzymatic targets, a small but increasing number of protein–protein inhibitors (PPIs) exist that have shown successes in clinical trials (Tse *et al.*, 2008; Gandhi *et al.*, 2011; Overington *et al.*, 2006). PPI discovery focuses on targeting binding clefts and ‘hot spots’ in protein–interaction interfaces at which small molecules or fragments can modulate their activity (Toogood, 2002).

Current therapeutic strategies for the treatment of pathogenic autoimmune diseases is to target proteins involved in the initiation event(s) of inflammation or ‘upstream’ events of the innate immune response. These ‘upstream’ effector proteins include cyclooxygenase 2 (Cox-2) and caspase-1 (interleukin-1 β converting enzyme; ICE) which respond to nonsteroidal anti-inflammatory drugs (NSAIDs) or specific ICE inhibitors, respectively, but suffer from side effects including colitis and others (Reuter *et al.*, 1996). Potential therapies exist that involve the use of antibodies directed against the interface of hIL-18 and hIL-18R α or the use of recombinant hIL-18BP, although these approaches face potential drawbacks in part owing to immune rejection (Hamasaki *et al.*, 2005). Identification of small molecules targeting the hIL-18 surface and disrupting the interaction between its receptors and IL-18BP could potentially bridge the gap from current therapeutics to the discovery of new therapeutics in the treatment of pathological diseases attributed to hIL-18 dysregulation. An important step in this process is obtaining crystals of apo hIL-18 protein or of hIL-18 in complex with small-molecule inhibitors. In this study, we employed surface-entropy reduction

(SER; Derewenda, 2004) to facilitate the crystallization of hIL-18 in low ionic strength conditions.

2. Materials and methods

2.1. SER design, protein expression and purification

Mature hIL-18 was cloned into a modified pET vector as a SUMO (small ubiquitin-like modifier) fusion protein with an N-terminal 6 \times His tag. We employed SER by targeting exposed lysine and glutamate patches on the surface of hIL-18, substituting these residues by alanine. The following mutations were performed using standard overlapping PCR (Shuldiner *et al.*, 1990): hIL-18 mutant I (K139A, K140A, E141A, E143A, L144A), mutant II (E128A, K129A, E130A, K135A), mutant III (K67A, E69A, K70A, I71A), mutant IV (mutant III plus E85A) and mutant V (P57R, K67A, E69A, K70A, I71A, S105R).

We expressed the recombinant fusion proteins in transformed *Escherichia coli* BL21 (DE3) Gold cells (Stratagene). The cells were grown at 37°C in Luria–Bertani (LB) broth until the OD₆₀₀ reached approximately 0.8–1.0, at which point the temperature was lowered to 18°C. Protein expression was induced after 1 h with a final concentration of 1 mM isopropyl β -D-1-thiogalactopyranoside (IPTG). The cells were allowed to continue to grow for an additional 18 h at 18°C and were then collected by centrifugation for 15 min at 5000g and stored at –20°C until use.

SUMO-hIL-18 mutants were purified at 4°C or on ice using a double Ni–nitrilotriacetic acid (Ni–NTA) procedure similar to that described by Krumm *et al.* (2008). Cells collected as above were suspended in buffer A (50 ml per litre of cultured cells) consisting of 20 mM Tris–HCl pH 7.0, 500 mM NaCl, 10% (w/v) glycerol, 20 mM imidazole, 5 mM β -mercaptoethanol (Sigma–Aldrich), 0.1 mM phenylmethanesulfonyl fluoride (Sigma–Aldrich). His-tagged fusion proteins were purified from the cells using high-pressure emulsification (Emulsiflex-C5, Avestin Inc., Ottawa, Ontario, Canada). The cell lysate was clarified by ultracentrifugation at 45 000g for 30 min and then batch-incubated for 4 h with 1 ml Ni–NTA (Qiagen) per litre of cultured cells. The Ni–NTA slurry was poured into a 20 ml disposable column (Bio-Rad), washed with 20 column volumes of buffer A and the bound protein was eluted with five column volumes of buffer A supplemented with 250 mM imidazole. The eluted fusion protein was co-dialyzed with ULP1 (ubiquitin-like specific protease 1) at a molar ratio of 100:1 (fusion:protease) in buffer A overnight to remove the SUMO moiety, exposing the authentic hIL-18 N-terminus (residue Tyr1). Cleaved protein mixtures were subsequently passed through a second subtracting Ni–NTA column and concentrated to approximately 1 mg ml^{–1} using a 15 kDa molecular-weight cutoff centrifugal concentrator (EMD Millipore). Concentrated hIL-18 mutants were further purified by size-exclusion chromatography using an ÄKTA purifier and a Superdex S200 16/300 column (GE Healthcare) loaded with 500 μ l sample at a flow rate of 0.4 ml min^{–1} in 20 mM Tris–HCl pH 7.0, 100 mM NaCl, 5 mM

Table 1

X-ray crystallographic data and refinement statistics.

Values in parentheses are for the highest resolution shell. The signal to noise $I/\sigma(I) > 2.0$ was at 2.95 Å for IL-18 SER mutant V.

	IL-18 SER mutant I	IL-18 SER mutant III	IL-18 SER mutant V
Data collection			
Beamline	19-ID, APS	19-ID, APS	19-ID, APS
Wavelength (Å)	0.97926	0.97929	0.97918
Space group	<i>P</i> 1	<i>P</i> 2 ₁ 2 ₁ 2 ₁	<i>P</i> 2 ₁ 2 ₁ 2 ₁
Unit-cell parameters			
<i>a</i> (Å)	33.0	54.5	42.7
<i>b</i> (Å)	42.3	55.0	52.0
<i>c</i> (Å)	52.3	113.0	123.4
α (°)	77.8	90	90
β (°)	83.6	90	90
γ (°)	67.1	90	90
Resolution (Å)	50–1.90 (1.97–1.90)	50–2.00 (2.03–2.00)	50–2.85 (2.90–2.85)
Total reflections	82848	172199	39780
Unique reflections	18429	24057	6953
Multiplicity	4.5 (3.3)	7.2 (6.9)	5.7 (4.2)
Completeness (%)	94.6 (81.6)	100 (100)	99.9 (98.3)
$\langle I/\sigma(I) \rangle$	19.8 (2.1)	30.0 (3.2)	9.0 (1.6)
$R_{\text{merge}}^{\dagger}$ (%)	10.5 (49.0)	7.5 (56.2)	19.3 (88.5)
Refinement statistics			
Resolution range used (Å)	50–1.91	50.0–2.00	33.0–2.85
No. of reflections used	17466	22784	6572
$R_{\text{work}}/R_{\text{free}}^{\ddagger}$ (%)	17.8/22.9	17.7/21.8	24.4/28.7
R.m.s.d., bond lengths (Å)	0.009	0.008	0.006
R.m.s.d., bond angles (°)	1.38	1.30	1.12
No. of atoms			
Protein	2507	2483	2426
Water	103	16	0
Average <i>B</i> factor§ (Å ²)			
Protein	35.8	42.5	50.1
Water	40.4	147.4	0
Ramachandran plot			
Preferred regions (%)	97.1	98.0	91.7
Allowed regions (%)	2.9	2.0	8.3

$\dagger R_{\text{merge}} = \frac{\sum_{hkl} \sum_i |I_i(hkl) - \langle I(hkl) \rangle|}{\sum_{hkl} \sum_i I_i(hkl)}$. $\ddagger R_{\text{work}} = \frac{\sum_{hkl} ||F_{\text{obs}}| - |F_{\text{calc}}||}{\sum_{hkl} |F_{\text{obs}}|}$. R_{free} was calculated using 5% of data for mutants I and III and 12.7% of data for mutant V. § Average *B* factors calculated using the *BAVERAGE* program from the *CCP4* suite.

β -mercaptoethanol. All mutant proteins eluted as a single monodisperse peak with an estimated molecular weight corresponding to monomeric hIL-18 in solution. The best fractions were concentrated as described above to saturation and were then flash-frozen in liquid nitrogen and stored at -80°C until use (Deng *et al.*, 2004).

2.2. Crystallization and structure determination

When compared with the wild-type protein, the SER hIL-18 mutants typically showed reduced solubility and could only be concentrated to 3–5 mg ml^{−1}, while the wild-type hIL-18 could be concentrated to 6–8 mg ml^{−1}. Concentrated hIL-18 mutants were initially screened against an array of commercially available sparse-matrix screens using the sitting-drop vapor-diffusion method employing a 96-head Gryphon robot (Art Robbins Instruments, USA). Crystals were optimized around initial hits using a grid-screen matrix of PEG and pH conditions. Mutant I crystallized in 47%(v/v) PEG 2000 monomethyl ether, 0.1 *M* HEPES pH 7.0, mutant III in

35%(v/v) PEG 3350, 0.1 *M* MES pH 6.5 and mutant V in 35%(v/v) PEG 3350, 0.1 *M* Tris pH 8.5, 0.1 *M* sodium acetate. Mutants II and IV did not yield reproducible quality crystals. Up to 5%(v/v) dimethyl sulfoxide (Sigma–Aldrich) was added to the crystallization drops to improve the crystal quality. Prior to data collection, the crystals were cryoprotected by briefly transferring them into a separate well containing mother liquor supplemented with 20%(v/v) glycerol.

Data from single crystals of mutants I, III and V were collected at beamline 19-ID at the Advanced Photon Source (APS), Argonne National Laboratory using an ADSC Quantum 315 detector system with 1° oscillation and 2–3 s exposure. All images were indexed, integrated and scaled with *HKL-2000/HKL-3000* (Otwinowski & Minor, 1997). Initial phases were determined by molecular replacement using *Phaser* (McCoy *et al.*, 2007) from the *CCP4* suite (Winn *et al.*, 2011) with hIL-18 from PDB entry 3f62 (Krumm *et al.*, 2008) as a search model. *PHENIX* (Adams *et al.*, 2010) and *REFMAC* (Murshudov *et al.*, 2011) were used for refinement and *Coot* (Emsley *et al.*, 2010) was used for iterative manual model building. The translation, libration and screw-rotation displacement (TLS) groups used in refinement were defined by the *TLMSD* server (Painter & Merritt, 2006). The final models have good refinement statistics as shown in Table 1. All molecular-graphics figures were generated with *PyMOL* (v1.7.4; Schrödinger).

3. Results and discussion

The first structure of hIL-18 was solved by solution NMR and other structures of hIL-18 have been determined either in complex with its cognate receptor(s), IL-18BPs or with hIL-18-specific antibodies (Kato *et al.*, 2003; Krumm *et al.*, 2008, 2012; Wei *et al.*, 2014; Argiriadi *et al.*, 2009; Tsutsumi *et al.*, 2014). Apo hIL-18 has been recalcitrant to crystallization. Although the crystal structure of apo hIL-18 has only recently been determined, the high ionic strength in the crystallization condition is not readily amenable for binding with potential ligands. In addition, the crystal packing buried the surface of hIL-18 that is involved in binding both its primary receptor (IL-18R α) and IL-18BP, preventing the possibility of soaking inhibitors into the existing crystals. We first attempted to crystallize wild-type hIL-18 in low ionic strength conditions as a basis for the design of small-molecule inhibitors targeting its interface surface. After exhaustive attempts to crystallize hIL-18, we were met without success and hIL-18 remained recalcitrant to crystallization. To overcome this hurdle, we employed the surface-entropy reduction (SER; Longenecker *et al.*, 2001; Derewenda, 2004) procedure by mutating spatially clustered lysine and glutamate residues to alanine(s). We visually inspected the structure of hIL-18 and mutated residues that were opposite the hIL-18–IL-18BP binding interface before hIL-18 binary and ternary receptor complexes recently became available. The identified residues are located at the bottom of the β -trefoil barrel opening on exposed loops connecting individual β -strands $\beta 5$ – $\beta 6$ (mutants III, IV and V), $\beta 10$ – $\beta 11$ (mutant II) and $\beta 11$ – $\beta 12$ (mutant I) (Figs. 1*b* and

1c; §2). The designed mutation sites were also confirmed with the *Surface Entropy Reduction prediction* server (Goldschmidt *et al.*, 2007). The identified mutations resulted in the successful crystallization of the three SER mutants that we have termed mutants I, III and V (Table 1).

SER mutants I and III crystallized in distinct crystallization conditions and in two different space groups. Mutant I crystallized in space group *P1* with two molecules in the asymmetric unit forming a nonphysiological dimer in a tail-to-tail orientation (Fig. 2*a*). The crystal contacts of mutant I involved the SER loop between $\beta 11$ and $\beta 12$ on molecule *A* of a given

asymmetric unit forming hydrophobic contacts with its crystallographic symmetry mate, with a BSA of 650 Å² as analyzed by the *PISA* server (Krissinel, 2010), and involved residues Ser7 and Leu9 located on $\beta 1$, Ile48 on $\beta 4$ and Asn87 located on the extended loop connecting $\beta 7$ and $\beta 8$ (Figs. 2*b* and 2*c*). Mutant III crystallized in space group *P2₁2₁2₁* with two molecules in the asymmetric unit forming a side-to-side homodimer in an opposing orientation to each other (one molecule facing up and the other facing down; Fig. 3*a*). The mutant III SER loop between $\beta 5$ and $\beta 6$ was also involved in crystal contacts between the two molecules in the asymmetric

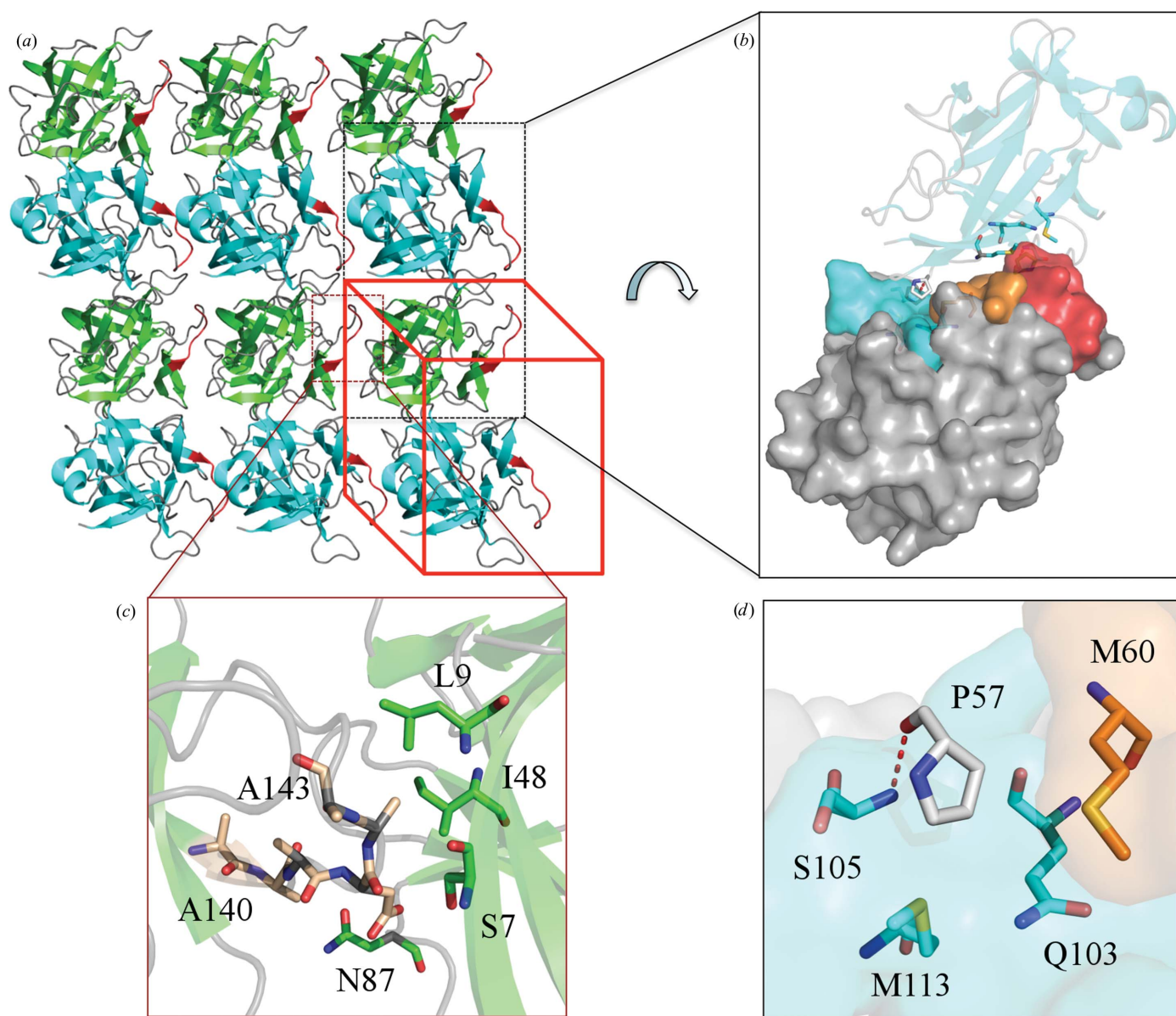


Figure 2

Crystal packing of hIL-18 SER mutant I. (*a*) hIL-18 mutant I with two molecules in the asymmetric unit is shown in cyan and green enclosed by the red outlined box. The view has been expanded to include symmetry-related molecules identifying crystal packing. Mutant I molecules are packed in a tail-to-tail orientation within the asymmetric unit. The SER loop from one of the symmetry-related molecules is colored red and outlined in the cayenne-colored box. (*b*) Surface representation of one mutant I molecule within the asymmetric unit (depicted similarly to as in Fig. 1*a*); the adjacent symmetry mate positioned such as to occlude the binding interface is shown in cyan. (*c*) Enlarged view of van der Waals interactions between the SER loop and the adjacent symmetry-mate molecule. (*d*) Enlarged view of the interactions at the interface between two overlapping molecules; hydrogen-bond interactions are shown as red dotted lines.

unit *via* close contact interactions between the cysteine residues (Cys68) of the respective SER loops, forming an intermolecular disulfide bond despite the presence of reducing conditions during protein purification. Hydrophobic interactions were also observed between the two molecules of the asymmetric unit, with a BSA of 546 Å², and involved SER loop residues Ala69 and Ala70 of molecule *A* interacting with the aliphatic side chains of Ser7, Leu9 and the main chain of Lys8 located on β 1 of molecule *B* (Figs. 3*b* and 3*c*). In both the mutant I and mutant III crystal structures the previously identified interface surface patches on hIL-18 involved in

IL-18BP or hIL-18R α binding were occluded by a crystallographic symmetry mate (Figs. 2*b* and 3*b*).

Further analysis of the SER mutant I and mutant III crystal structures revealed a nearly symmetrical crystal-packing interaction involving several binding-interface residues which are also found in the recent apo hIL-18 structure (Kimura *et al.*, 2014; Tsutsumi *et al.*, 2014). Surface residue Pro57 (site A) of molecule *A* participates in van der Waals interactions with the aliphatic side chains of Met60 (site B), Gln103, Ser105 and Met113 (all in site C) of molecule *B*. Residues Pro57 and Ser105 also participated in hydrogen-bonding interactions

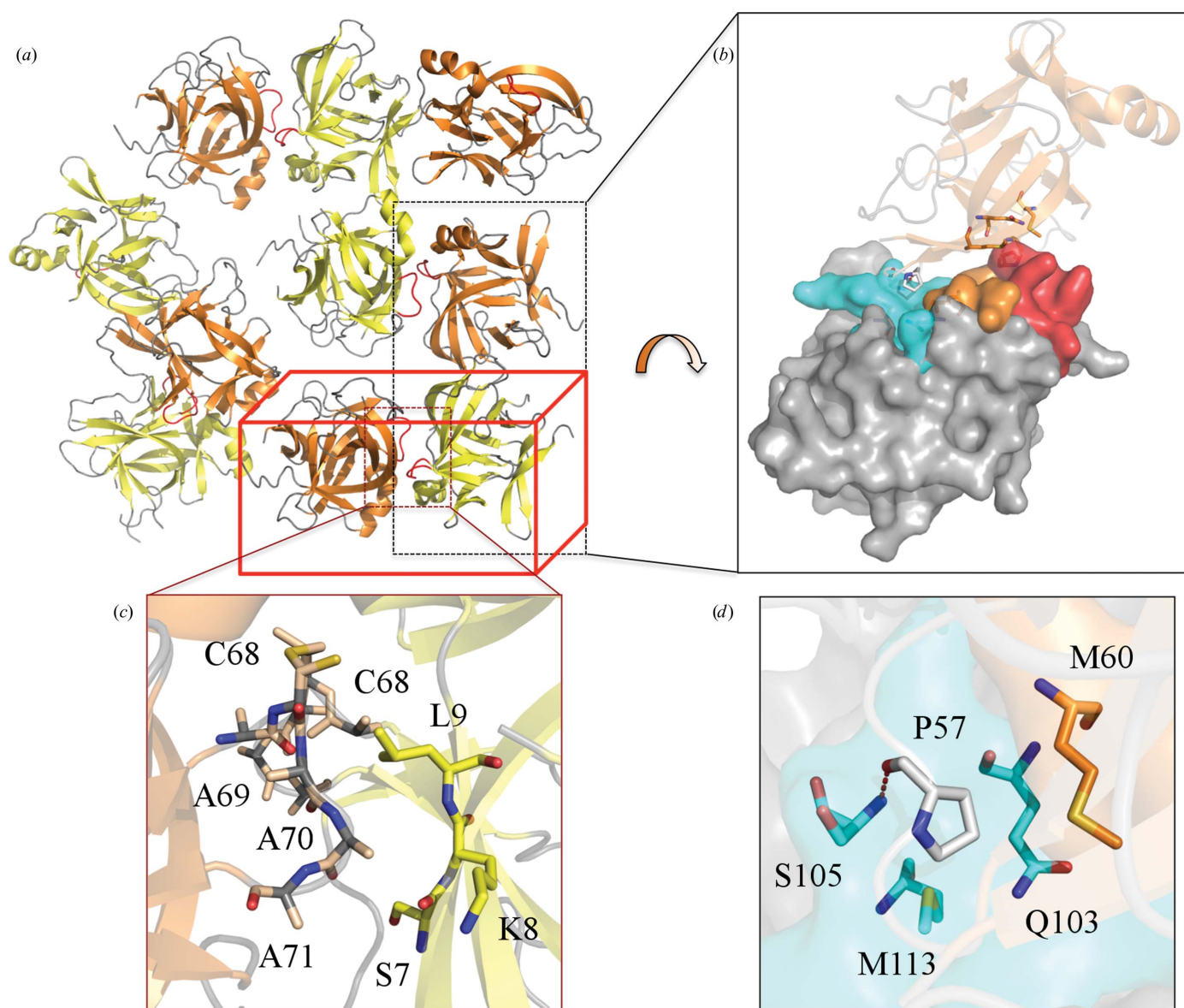


Figure 3

Crystal packing of hIL-18 SER mutant III. (a) Mutant III with two molecules in the asymmetric unit is shown in orange and yellow enclosed by the red outlined box. The view has been expanded to include symmetry-related molecules identifying crystal packing. Mutant III molecules are packed in a side-to-side orientation forming a homodimer with one molecule facing up and the other facing down relative to each other within the asymmetric unit. The respective SER loops making contact with each other are colored in red and outlined in the cayenne-colored box. (b) Surface representation of one mutant III molecule (depicted similarly to as in Fig. 1*a*); the adjacent symmetry mate positioned such as to occlude the binding interface is shown in orange. (c) Enlarged view of van der Waals interactions between the SER loops within the asymmetric unit. Also identified is the intermolecular disulfide bond between the SER loops. (d) Enlarged view of the interactions at the interface between the two molecules; hydrogen-bond interactions are shown as red dotted lines.

between their main-chain O and N atoms, respectively (Figs. 2*d* and 3*d*). We hypothesized that disrupting the Pro57 and Ser105 interactions would result in a different crystal packing avoiding the unwanted homodimer structure. We generated a new mutant, SER mutant V, by introducing additional P57R and S105R mutations into mutant III. Mutant V also crystallized in a high concentration of PEG 3350 in space group $P2_12_12_1$ similar to mutant III, but with significantly different unit-cell parameters (Table 1).

Upon obtaining a good molecular-replacement solution, we found that the P57R and S105R mutations indeed generated

new crystal lattice packing also containing two molecules within the asymmetric unit. The crystal lattice packing displays a head-to-side abutting orientation between molecule A of a given asymmetric unit and molecule B of the adjacent asymmetric unit (Figs. 4*a* and 4*b*). The two molecules within the asymmetric unit are nearly parallel to each other, with a slight twist relative to each other. Similar to mutant III, the molecules form a side-to-side homodimer but with both molecules in the asymmetric unit adopting the same orientation (facing in the same direction relative to each other). Also similar to mutant III, the SER loop between $\beta 5$ and $\beta 6$ is involved in

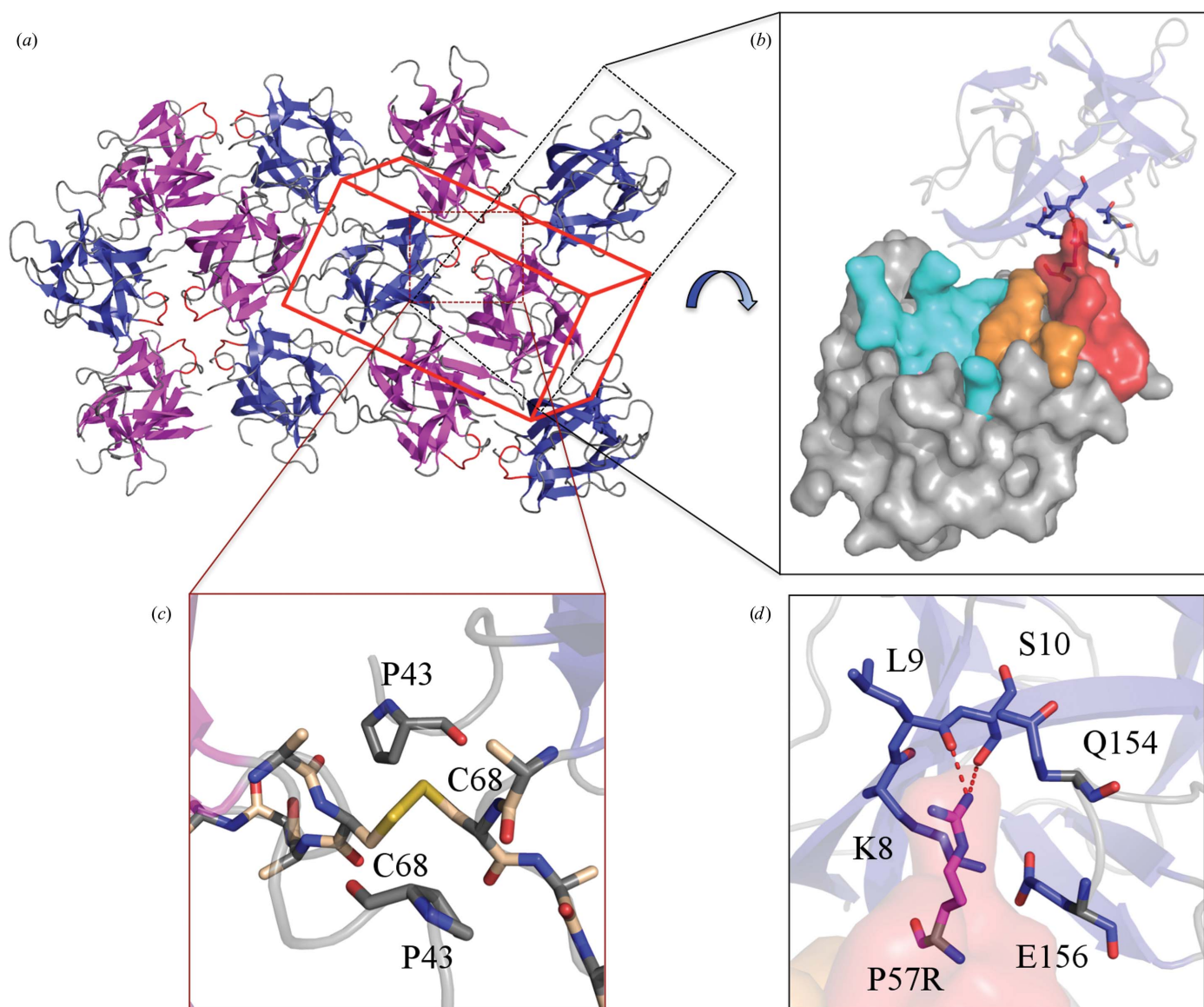


Figure 4

Crystal packing of hIL-18 SER mutant V. (*a*) Mutant V with two molecules in the asymmetric unit is shown in magenta and blue enclosed by the red outlined box. The view has been expanded to include symmetry-related molecules identifying crystal packing. Mutant V molecules are packed in a side-to-side orientation almost parallel to each other, with both molecules facing in the same direction relative to each other within the asymmetric unit. The SER loops from each molecule making contact with each other are colored in red and outlined in the cayenne-colored box. The molecules interact predominantly through a disulfide bond between the two SER loops. (*b*) Surface representation of one mutant V molecule (depicted similarly to as in Fig. 1*a*); an adjacent symmetry-related molecule positioned such as to allow a near completely open interface is shown in blue. (*c*) Enlarged view showing van der Waals interactions between the SER loops. (*d*) Enlarged view of interactions at the interface between the two molecules; hydrogen-bond interactions are shown as red dotted lines.

crystal contacts with a BSA of 386 \AA^2 between the two molecules of the asymmetric unit *via* close contact interactions between the cysteine residues (Cys68) of the respective SER loops, forming an intermolecular disulfide bond. Additional SER loop interactions involve van der Waals interactions between C^α of Cys69 and the aliphatic side chain of Pro43 located on the loop connecting $\beta 4$ and $\beta 5$ (Fig. 4d). The side chain of P57R of molecule *A* is involved in hydrogen bonding and van der Waals interactions with residues Lys8, Leu9 and Ser10 of $\beta 1$ and the C-terminal residues Gln154 and Glu156 of molecule *B* from an adjacent asymmetric unit (Fig. 4d). P57R of molecule *B* and S105R from both molecules within the given asymmetric unit are disordered and do not appear to make any interactions with neighboring molecules. In this crystal-packing pattern, the targeted hIL-18 surface on one molecule is mostly open, while more than 50% of the surface on the other molecule is also open and exposed (Fig. 4b).

4. Conclusion

Through surface-entropy reduction and rational protein design, we have successfully crystallized an otherwise recalcitrant protein in low ionic strength conditions. The SER mutated residues were found to be consistently involved in crystal lattice contacts. Rational protein engineering of the pliable interface of hIL-18 has enabled the crystallization of this previously occluded interface preventing the identification and design of inhibitors targeting the interface of hIL-18. The opportunity now exists to further exploit the hIL-18 interface by providing a platform for structure-based drug design.

Acknowledgements

The authors wish to thank the staff of beamline 19-ID at the Advanced Photon Source for their generous support. This research used resources of the Advanced Photon Source, a US Department of Energy (DOE) Office of Science User Facility operated for the DOE Office of Science by Argonne National Laboratory under Contract No. DE-AC02-06CH11357. This study was supported by NIH grants AI113539 (JD) and AI079217 (YX) and also by Oklahoma Center for the Advancement of Science and Technology (OCAST) under project HR14-068 (JD).

References

- Adams, P. D. *et al.* (2010). *Acta Cryst.* **D66**, 213–221.
Argiriadi, M. A., Xiang, T., Wu, C., Ghayur, T. & Borhani, D. W. (2009). *J. Biol. Chem.* **284**, 24478–24489.

- Boraschi, D. & Dinarello, C. A. (2006). *Eur. Cytokine Netw.* **17**, 224–252.
Deng, J., Davies, D. R., Wisedchaisri, G., Wu, M., Hol, W. G. J. & Mehlh, C. (2004). *Acta Cryst.* **D60**, 203–204.
Derewenda, Z. S. (2004). *Structure*, **12**, 529–535.
Dinarello, C. A. (1999a). *J. Allergy Clin. Immunol.* **103**, 11–24.
Dinarello, C. A. (1999b). *Methods*, **19**, 121–132.
Emsley, P., Lohkamp, B., Scott, W. G. & Cowtan, K. (2010). *Acta Cryst.* **D66**, 486–501.
Esteban, D. J. & Buller, R. M. (2004). *Virology*, **323**, 197–207.
Gandhi, L. *et al.* (2011). *J. Clin. Oncol.* **29**, 909–916.
Goldschmidt, L., Cooper, D. R., Derewenda, Z. S. & Eisenberg, D. (2007). *Protein Sci.* **16**, 1569–1576.
Hamasaki, T., Hashiguchi, S., Ito, Y., Kato, Z., Nakanishi, K., Nakashima, T. & Sugimura, K. (2005). *J. Biochem.* **138**, 433–442.
Kato, Z., Jee, J., Shikano, H., Mishima, M., Ohki, I., Ohnishi, H., Li, A., Hashimoto, K., Matsukuma, E., Omoya, K., Yamamoto, Y., Yoneda, T., Hara, T., Kondo, N. & Shirakawa, M. (2003). *Nature Struct. Biol.* **10**, 966–971.
Kimura, T., Tsutsumi, N., Arita, K., Ariyoshi, M., Ohnishi, H., Kondo, N., Shirakawa, M., Kato, Z. & Tochio, H. (2014). *Acta Cryst.* **F70**, 1351–1356.
Krissinel, E. (2010). *J. Comput. Chem.* **31**, 133–143.
Krumm, B., Meng, X., Li, Y., Xiang, Y. & Deng, J. (2008). *Proc. Natl Acad. Sci. USA*, **105**, 20711–20715.
Krumm, B., Meng, X., Wang, Z., Xiang, Y. & Deng, J. (2012). *PLoS Pathog.* **8**, e1002876.
Longenecker, K. L., Garrard, S. M., Sheffield, P. J. & Derewenda, Z. S. (2001). *Acta Cryst.* **D57**, 679–688.
McCoy, A. J., Grosse-Kunstleve, R. W., Adams, P. D., Winn, M. D., Storoni, L. C. & Read, R. J. (2007). *J. Appl. Cryst.* **40**, 658–674.
Meng, X., Leman, M. & Xiang, Y. (2007). *Virology*, **358**, 211–220.
Murshudov, G. N., Skubák, P., Lebedev, A. A., Pannu, N. S., Steiner, R. A., Nicholls, R. A., Winn, M. D., Long, F. & Vagin, A. A. (2011). *Acta Cryst.* **D67**, 355–367.
Okamura, H. *et al.* (1995). *Nature (London)*, **378**, 88–91.
Otwinski, Z. & Minor, W. (1997). *Methods Enzymol.* **276**, 307–326.
Overington, J. P., Al-Lazikani, B. & Hopkins, A. L. (2006). *Nature Rev. Drug Discov.* **5**, 993–996.
Painter, J. & Merritt, E. A. (2006). *Acta Cryst.* **D62**, 439–450.
Reuter, B. K., Asfaha, S., Buret, A., Sharkey, K. A. & Wallace, J. L. (1996). *J. Clin. Invest.* **98**, 2076–2085.
Shuldiner, A. R., Scott, L. A. & Roth, J. (1990). *Nucleic Acids Res.* **18**, 1920.
Stumpf, M. P., Thorne, T., de Silva, E., Stewart, R., An, H. J., Lappe, M. & Wiuf, C. (2008). *Proc. Natl Acad. Sci. USA*, **105**, 6959–6964.
Toogood, P. L. (2002). *J. Med. Chem.* **45**, 1543–1558.
Tse, C. *et al.* (2008). *Cancer Res.* **68**, 3421–3428.
Tsutsumi, N., Kimura, T., Arita, K., Ariyoshi, M., Ohnishi, H., Yamamoto, T., Zuo, X., Maenaka, K., Park, E. Y., Kondo, N., Shirakawa, M., Tochio, H. & Kato, Z. (2014). *Nature Commun.* **5**, 5340.
Wei, H., Wang, D., Qian, Y., Liu, X., Fan, S., Yin, H.-S. & Wang, X. (2014). *FEBS Lett.* **588**, 3838–3843.
Winn, M. D. *et al.* (2011). *Acta Cryst.* **D67**, 235–242.
Xiang, Y. & Moss, B. (2001a). *J. Biol. Chem.* **276**, 17380–17386.
Xiang, Y. & Moss, B. (2001b). *J. Virol.* **75**, 9947–9954.